JOURNAL OF MATERIALS RESEARCH AND TECHNOLOGY 2021;15:5197–5212

Available online at www.sciencedirect.com

jmr&t Journal of Materials Research and Technology

journal homepage: www.elsevier.com/locate/jmrt

Original Article

TiO_2 nanostructured coated functionally modified and composite electrospun chitosan nanofibers membrane for efficient photocatalytic degradation of organic pollutant in wastewater

Fahad A. AlAbduljabbar [a], *Sajjad Haider* [b,*], *Fekri Abdulraqeb Ahmed Ali* [b], *Abdulaziz A. Alghyamah* [b], *Waheed A. Almasry* [b], *Raj Patel* [a], *Iqbal M. Mujtaba* [a,**]

[a] *Department of Chemical Engineering, Faculty of Engineering & Informatics, University of Bradford, Bradford BD7 1DP, West Yorkshire, UK*

[b] *Department of Chemical Engineering, College of Engineering, King Saud University, P.O. Box 800, Riyadh, 11421, Saudi Arabia*

ARTICLE INFO

Article history:
Received 7 July 2021
Accepted 26 October 2021
Available online 30 October 2021

Keywords:
Modified nanofibers
Electrospun membrane
TiO_2/Chitosan composite
TiO_2 coated chitosan modified nanofibers
Photocatalysis

ABSTRACT

In this study, we prepared chitosan (Cs_P) nanofibers (NFs) membrane by electrospinning. The Cs_P NFs membrane was then chemically functionalized (CsF) by a novel stepwise chemical process. The CsF NFs membrane was electrospray with TiO_2 nanoparticles (NPs) to prepare the CsF_Coa NFs membrane. A second NFs membrane with embedded TiO_2 NPs (Cs_Co) was also prepared by electrospinning. The TiO_2 NPs, Cs_P, CsF s, CsF_Coa NFs, and Cs_Co NFs membranes were analyzed by standard spectroscopic, microscopic, X-ray, and thermal methods. Fourier transform infrared (FTIR) analysis confirmed the incorporation of the new functional group into the Cs structure. X-ray photoelectron spectroscopy (XPS) data confirmed the FTIR results and the fabrication of the CsF NFs membrane. Scanning electron microscope (SEM) micrographs showed a smooth morphology for the Cs_P NFs membrane and a denser morphology for the CsF NFs membrane (NFs swelled with functionalization). The SEM micrographs also showed a dense cloud of TiO_2 NPs on the surface of the Cs_Coa NFs membrane. Transmission electron microscope (TEM) showed that the particle size of TiO_2 NPs varied between 20 and 35 nm and tended to be spherical. The X-ray diffraction (XRD) pattern confirmed the existence of the anatase phase of the TiO_2 NPs. The presence of TiO_2 in the Cs_Coa and Cs_Co NFs membranes was also confirmed by energy-dispersive x-ray spectroscopy (EDX). Surface profilometry confirmed an increase in the surface roughness of the CsF and Cs_Coa NFs membranes. Brunauer–Emmett–Teller (BET) analysis revealed that the isotherms and hystereses for all NFs membranes were of the IV and H3 types, respectively, corresponding to mesopores and slit pores. The higher photocatalytic activity of the Cs_Coa NFs membrane (89%) compared to the Cs_Co NFs

* Corresponding author.
** Corresponding author.
E-mail addresses: shaider@ksu.edu.sa (S. Haider), i.m.mujtaba@bradford.ac.uk (I.M. Mujtaba).

https://doi.org/10.1016/j.jmrt.2021.10.119

membrane (40%) was attributed to a balance between the short band gap, high surface roughness, and lower surface area.

1. Introduction

The environmental risks associated with various types of pollution were reassessed by researchers after a decade, both locally and internationally. This was done because the environment was increasingly affected by the accumulation of organic pollutants resulting not only from the exponential growth of developing technologies and industrialization, but also from changes in human lifestyles [1]. In addition, several countries experienced rapid urbanization. With increasing urbanization, the challenges of providing clean and healthy water to a rapidly growing population have become even more complex. Wastewater is any water that contains liquid wastes and is directly discharged into freshwater from households, commercial establishments, industries, etc. Direct discharge of wastewater from households and industries with minimal treatment into watercourses and waterways has resulted in polluted raw water [2]. This water has hindered the use of clean and safe water in everyday activities such as cooking, washing clothes, cleaning dirt, and drinking. The effects of increasing water pollution pose a threat to the health of living beings, be it humans, animals, or plants. Such water causes toxicity and transmission of diseases in living beings. Various pollutants present in wastewater can cause diseases depending on the form of the pollutants. Current wastewater treatment methods are not capable of removing pollutants from water. There is no treatment technology that is universally applicable for the removal of all pollutants. As the environment continues to deteriorate, membrane technology promises to become an innovative treatment and recovery method for improving and expanding wastewater treatment. This type of technology is becoming increasingly attractive to wastewater researchers due to its many advantages over conventional methods. Therefore, membrane systems are expected to improve the effectiveness of treating pollutants in wastewater treatment. However, they also have some disadvantages, the most important of which is membrane fouling.

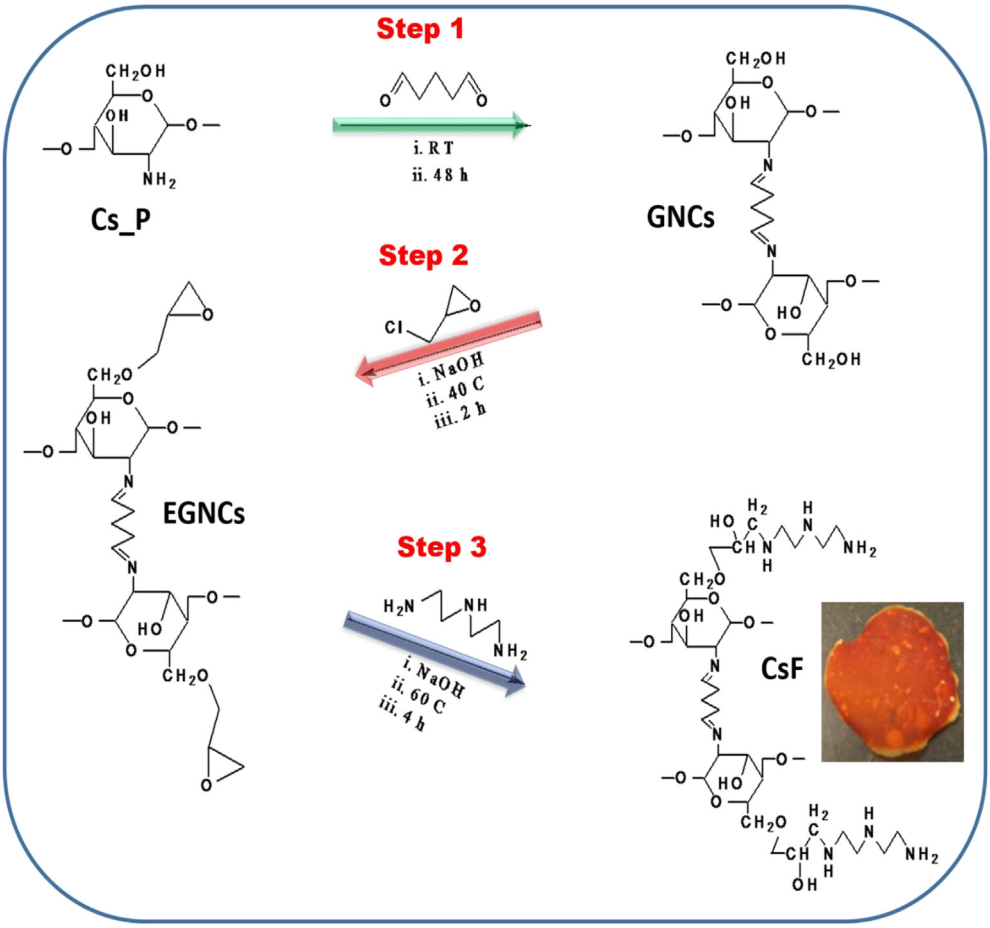

Fig. 1 – Scheme illustrating the steps of the synthesis of CsF NFs membrane.

Fouling reduces permeate flux and membrane separation efficiency. Photodegradation of pollutants in wastewater is considered as one of the best methods not only to reduce membrane fouling but also to control micropollutants [3]. Photodegradation is an effective and advanced oxidation process (AOP) for the treatment of toxic pollutants, mainly because of its high efficiency, low cost, and low environmental impact [3,4]. Chemical constituents are usually removed from commercial and municipal wastewater using AOPs. AOPs processes are promising methods for the treatment of non-biodegradable or poorly degradable organic compounds present in wastewater [5]. In photocatalysis, the membrane serves as a separating medium and the catalyst ensures the degradation of complex pollutant molecules into simple non-toxic molecules. Photocatalysis is simple, inexpensive, and can be easily applied on an industrial scale. In the photocatalytic process, a semiconducting material is used as a catalyst to absorb light. Nowadays, ceramic materials with nanostructure are increasingly used as catalysts to increase the efficiency of the process because small particles provide much a larger surface area for the reaction between pollutants and catalyst. Due to the larger surface area, nanomaterials have the potential to reduce the toxicity of pollutants to lower and safer levels. For this reason, the small pore size and high surface area to volume ratio make the electrospun NFs membrane a cutting-edge technology. In addition, NFs membrane has flexibility, surface functionalities, high surface to length ratio, and good porosity. These excellent properties of NFs technology have led to its use in a wide range of critical applications. Titanium dioxide (TiO_2), used in photocatalytic processes, is an excellent semiconductor for removing organic and inorganic pollutants from water and air. Due to its low band gap energy and high photocatalytic activity, titanium dioxide has been used as a photocatalysts in many studies [6]. Moreover, several studies have reported the modification of titanium dioxide [7]. The modification of photocatalyst not only changes the process and kinetics under radiation, but also adds an activity in visible light. The photocatalytic activity of the photocatalyst mainly depends on the substrate and the conditions of the modification process. The use of NFs as substrate is the most impressive modification of TiO_2 photocatalyst [8]. The use of NFs in photocatalysis increases the photodegradation efficiency. The increase in photodegradation efficiency results from the enhanced surface interactions between the catalyst and the pollutants. Many experts have been working on the degradation of dye pollutants in recent years. The photocatalytic process using TiO_2 as photocatalyst is the most efficient method. Many studies have been published in the literature on the use of TiO_2 nanostructures as photocatalysts. However, there are very few reports on the use of NFs and TiO_2 [9,10]. This research area is still novel: therefore, work is needed to explore the full potential of this area.

In this work, we fabricated a Cs_P NFs membrane by electrospinning. The Cs_P NFs membrane was then chemically functionalized (CsF) by a novel stepwise chemical process. The CsF NFs membrane was electrosprayed with TiO_2 NPs to prepare CsF_Coa NFs membrane. A second composite

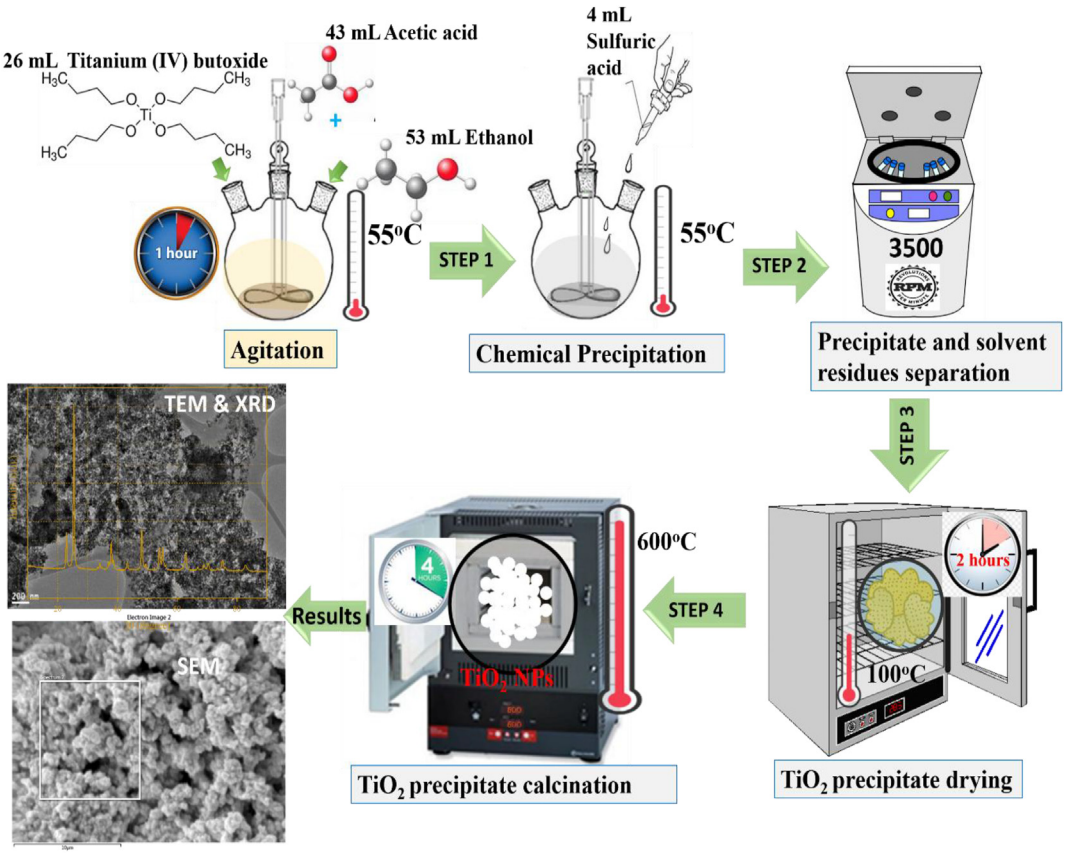

Fig. 2 – Scheme showing the steps of the synthesis of nanocrystalline anatase TiO_2 NPs.

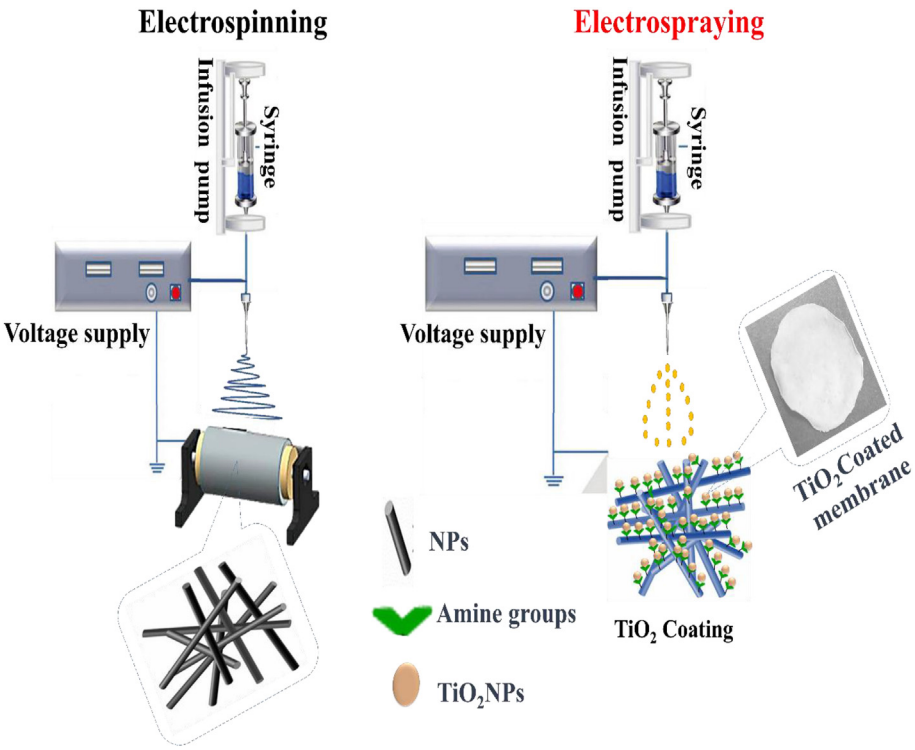

Fig. 3 – Schematic of electrospinning for the Cs_P and Cs_Co NFs membranes and electrospyying of TiO_2 onto the CsF NFs membrane.

membrane (Cs_Co) with TiO_2 NPs embedded in the NFs was also prepared by electrospinning. The CsF_Coa and Cs_Co NFs membranes were used for the degradation of methylene blue dye. To the best of our knowledge, there is no report of a similar study is in the literature.

2. Materials and methods

2.1. Materials

Cs powder (Medium molecular weight), trifluoroacetic acid (TFA (CF_3COOH)), diethylenetriamine (DETA ($C_4H_{13}N_3$)), titanium (IV)-n-butoxide ($Ti(C_4H_9O)_4$), glacial acetic acid (CH_3COOH), sulfuric acid (H_2SO_4), and sodium hydroxide (NaOH) were supplied by Sigma–Aldrich. Epichlorohydrin (ECH (C_3H_5ClO)) and absolute ethanol (C_2H_5OH) were purchased from Alfa Aesar and Paneac Quimica SLU, respectively. Glutaraldehyde (GTA ($C_5H_8O_2$)) and anhydrous potassium carbonate (K_2CO_3) were purchased from Loba Chemie. All materials were of analytical grade and were used without further purification. Distilled water was used in the preparation of the K_2CO_3 solution. To minimize the membrane shrinkage during the reactions, locally manufactured Teflon frames were used to fix the corners of the NFs membrane.

2.2. Methods

2.2.1. Preparation Cs_P NFs membrane

The Cs solution (6 wt%) was prepared by adding 1.8 g of Cs powder in 30 mL of TFA. The Cs was dissolved in TFA for 5 h on a magnetic stirrer (model Cerastir 30539) at room temperature. Stirring continued for 5 h to obtain a homogeneous solution. After dissolution, the solution was filtered with a sieve (0.063 mm pore size) to remove visible undissolved particles. Following the standard electrospinning procedure: The Cs solution was added to a 30 mL plastic syringe with a stainless steel needle of 0.8mm diameter. The syringe was placed in a control flow pump. The needle of the syringe was connected to a high voltage supply. The Cs solution was electrospun at previously optimized conditions [11] using an electrospinning machine (NANON-01A, MCC, JAPAN). The speed of the cylindrical collector was 50 revolutions per minute (rpm). After electrospinning: the NFs were removed from the aluminum foil (rolled over the rotating drum), dried in the vacuum oven (model DP63, Yamata Scientific Co. Ltd) at 60 °C and - 0.1 MPa, and stored in a desiccator for functionalization and characterization.

2.2.2. Functionalization of the Cs_P to CsF NFs membrane

2.2.2.1. Synthesis of the crosslinked (GNCs) NFs membrane. The GNCs NFs membrane was prepared by exposing the Cs_P NFs membrane to GTA vapors and then neutralizing it with a salt. For this purpose, the Cs_P NFs membrane was fixed in a Teflon frame and placed on a porous ceramic shelf of the desiccator. A Petri dish containing 25% aqueous GTA solution was placed on the bottom of the desiccator. The desiccator was closed with a lid. The crosslinking reaction was carried out for 48 h at room temperature. The membrane produced was named as GTA cross-linked chitosan (GCs). GCs, after completion of reaction was removed from the desiccator and added to an aqueous 1 M. L^{-1} K_2CO_3

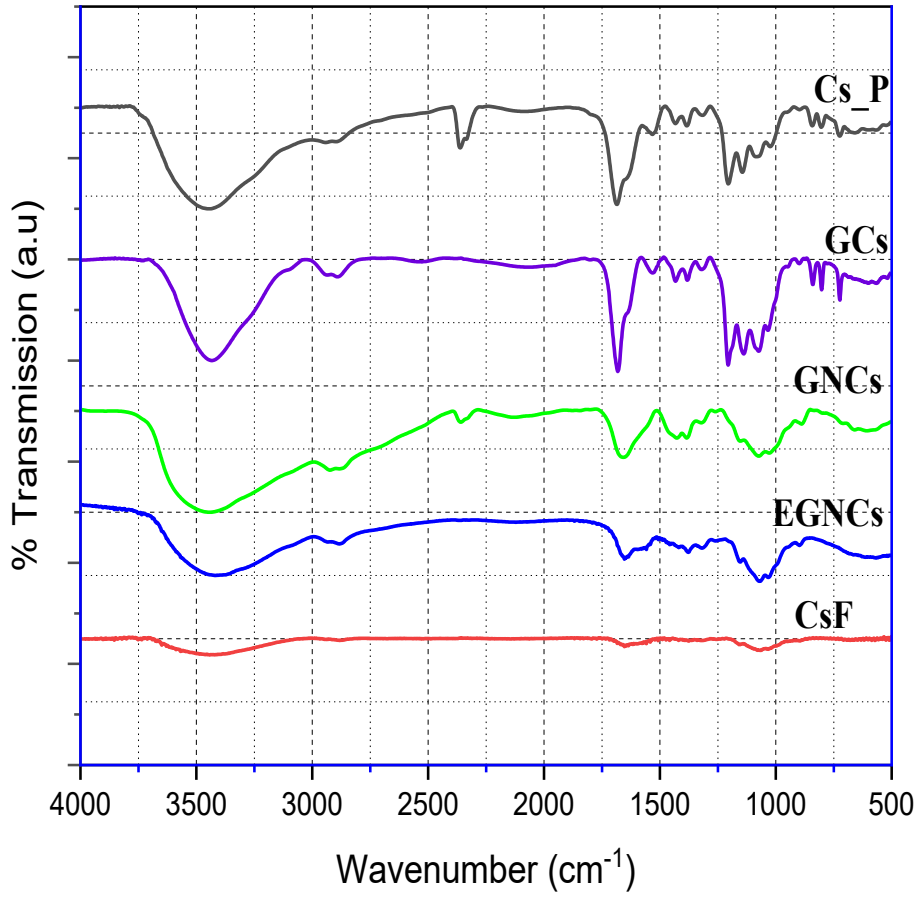

Fig. 4 – FTIR analysis of the NFs membranes involved in the functional process.

solution. The reaction was carried out for 3 h at room temperature. After completion of the reaction, the GNCs NFs membrane was removed from the aqueous solution and washed with distilled water to pH 7. The membrane was then dried, first at room temperature for 24 h and then in an oven at 100 °C for 24, and stored in a zipper bag for the next reaction step.

2.2.2.2. *Synthesis of epichlorohydrin(Ep) immobilized (EGNCs) NFs membrane*. **E**GNCs NFs membrane was synthesized by adding GNCs NFs membrane to a mixture of 0.01M (50 mL) Ep solution and 0.067 M of NaOH solution (pH 10). The reaction was carried out for 2 h (with constant stirring) at 40 °C. After completion of the reaction, the **E**GNCs membrane was rinsed with distilled water to remove the access reactant and stored for the final step.

2.2.2.3. *Synthesis CsF NFs membrane*. **CsF** NFs membrane was synthesized by adding **E**GNCs NFs membrane in 50 mL DETA solution. The DETA solution was prepared at a ratio of 1:10 (v/v) in 4 M L^{-1} NaOH. The reaction was carried out for 4 h with constant agitation and at 60 °C. After completion of the reaction, the **CsF** membrane was removed from the mixture and washed repeatedly first with ethanol and then with distilled water. The synthesis of **CsF** NFs membrane is shown in Fig. 1. The membrane **CsF** was stored in a zipper bag for electrospray of the TiO_2 NPs onto the membrane.

2.2.3. *Synthesis of TiO_2*

TiO_2 NPs were synthesized by the chemical precipitation method. Briefly, 26 mL titanium (IV)-n-butoxide (Ti (OBu) 4), 53 mL ethanol, 43 mL glacial acetic acid, and 4 mL sulfuric acid were carefully measured. All solutions, except sulfuric acid, were mixed in a reaction container for 1 h with constant stirring and at 55 °C. After mixing, sulfuric acid was added dropwise to the mixture using a dropper. The reaction was stopped after gel formation. To remove the remaining solvents from the gel, the mixture was centrifuged at 3500 rpm. Finally, the gel was dried at 100 °C for 2 h and calcined for 6 h at 600 °C to obtain the desired nanocrystalline anatase TiO_2 NPs. Fig. 2 shows the method used to prepare nanocrystalline anatase TiO_2 NPs.

2.2.4. *Preparation of Cs_Coa NFs membrane*

2 wt. % TiO_2 NPs were first suspended in 10 mL of TFA solvent. The suspension was then ultrasound sonicated for 5 min. After sonication, the solution was added to a 10 mL plastic syringe. The plastic syringe was placed into a control flow pump. The suspension was then electrospray (Fig. 3) onto the surface of the CsF NFs membrane using an electrospinning machine (NANON-01A, MCC, JAPAN). The speed of the cylindrical collector was maintained at 50 rpm. The applied voltage was 20 kV, the flow rate was 0.8 mL/h, and the distance between the collector and the needle tip was 100 mm. Fig. 2 shows all synthetic steps and the coating of the NFs membrane.

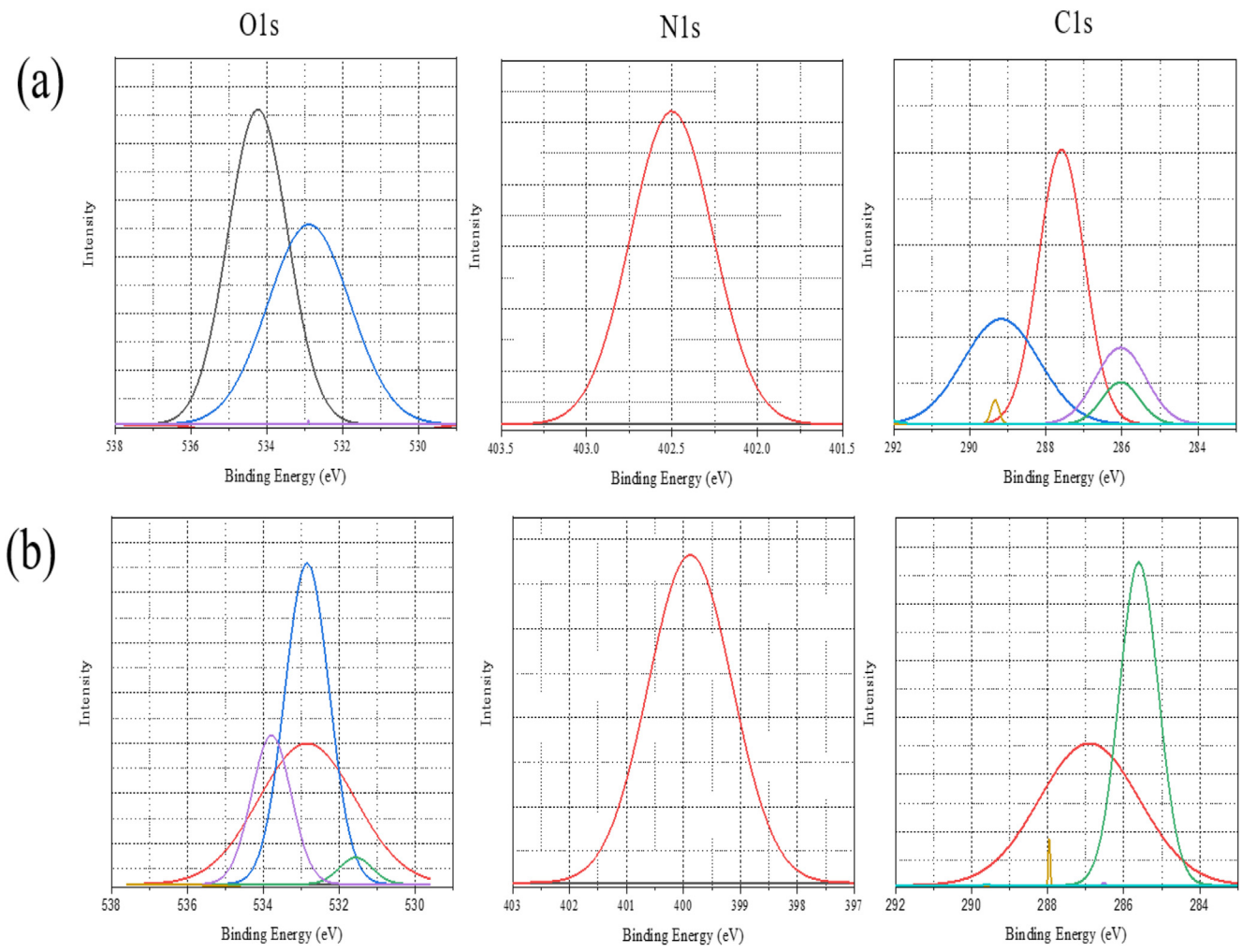

Fig. 5 – XPS results of the surface O1s, N1s, and C1s spectra of (a) Cs_P and (b) CsF NFs membranes.

2.2.5. *Preparation of Cs_Co NFs membrane*

The Cs solution (6 wt%) was prepared by adding 1.8 g of Cs powder in 30 mL of TFA. The Cs was dissolved in TFA for 5 h at room temperature on a magnetic stirrer (model Cerastir 30539). Stirring was continued for 5 h to obtain a homogeneous solution. After dissolution, the solution was filtered with a sieve (0.063 mm pore size) to remove visible undissolved particles. Different wt% (0.2, 1, and 2) TiO_2 NPs were added separately to the 6 wt% Cs solutions. According to the standard electrospinning procedure: The Cs/TiO_2 solutions were added separately to a 30 mL plastic syringe with a stainless steel needle of 0.8 mm diameter. The syringe was placed in a controlled flow pump. The needle of the syringe was connected to a high-voltage source. The Cs solution was electrospun at previously optimized conditions (Fig. 3) [11].

3. Characterization

FTIR spectrometer (Bruker Vertex 70) was used to study the FTIR spectra of Cs powder, the membranes prepared in the different functionalization steps (GCs, GNCs, EGNC), and CsF NFs membrane. The spectra of the membranes were recorded in the range of 4000–500 cm^{-1}. Prior to FTIR analysis, the samples were crushed, mixed, and pressed into KBr pellets by mechanical pressure. Data were processed with Bruker's OPUS 6.0 software using the rubber band method (removal of CO_2 and H_2O bands). X-ray photoelectron spectroscopy (XPS) analyzes were performed using an electron spectroscopy chemical analysis (ESCA) system (model VG 3000) with monochromatic Mg-Kα line (1253.6 eV) radiation. The TGA Q50 (TA Instruments) was used to study the thermal behavior of the CS powder, the membranes prepared in the different functionalization steps (GNCs, EGNC) CS_P, and CsF NFs membranes. Each sample was placed in a platinum plate, weighed, and then heated from 25 °C to 600 °C under nitrogen at a rate of 10 °C/min. SEM (JSM-7600 F) was used to study the surface morphologies of Cs_P, CsF, CsF_Coa, and Cs_Co NFs membranes. The membrane samples were attached to holders with carbon tape and then placed in the sputtering machine for platinum coating. The platinum-coated samples were examined using SEM under a high vacuum. The morphology and size of the synthesized TiO_2 NPs were examined using TEM (JEM-2100F). Micromeritics (Gemini VII, 2390 surface area, and

porosity USA) was used to determine the surface area, pore size, pore volume, and total pore area of Cs_P, CsF, CsF_Coa, and Cs_Co NFs membranes. Prior to analysis, the sample was degassed at 150 °C for 120 min under N_2 flow to remove moisture and vapors. Adsorption–desorption isotherms were studied at STP in the relative pressure range of 0.0–0.1. XRD diffractograms were recorded at 40 kV and 30 mA with Cu Kα radiation (1.540 Å). Diffractograms were recorded using an X-ray diffractometer (Bruker AXS D8 Advance XRD) at 2θ° ranging from 20° to 80°. Surface roughness was determined using the optical microscope contour GT-K 3D (Bruker®), non-contact 3D surface metrology and interferometry. Vertical scanning interferometry with a 5x Michelson magnification objective, a field of view of 1.0 1.0 mm^2, a Gaussian regression filter, a scan speed of 1x, and a threshold of 4 was used to measure the samples. Samples were placed on the stage and manually adjusted to obtain an image on the screen. The microscope is controlled by Vision 64 software (Bruker®), which handles instrument settings, data analysis, and graphical output. Vertical scanning interferometry was used for the measurement, which employs broadband (usually white) light source and is suitable for measuring objects with rough surfaces and adjacent pixel-height variations greater than 135 nm. Each sample was scanned at three different locations with three intervals and then averaged to obtain the roughness value (Ra).

4. Degradation of methylene blue dye

Different weights (25, 50, 100 mg) of CsF_Coa NFs membrane were added separately to 100 mL of the 5, 10, and 15 ppm methylene blue dye solutions. Based on the results, the optimal dose (100 mg) of CsF_Coa and concentration (10 ppm) of methylene blue were determined. After optimization, 100 mg of the CsF_Coa and Cs_Co NFs (Cs _Co had different wt % of TiO_2 NPs 0.2, 1, and 2) membranes were added separately to 100 mL of a 10 ppm methylene blue solution. Each mixture was placed in a photocatalysis reactor with an incandescent filament bulb (450 W) as the UV/visible light source. The concentration of methylene blue in the solution was measured every 30 min using a UV/visible spectrophotometer. The data of photocatalytic degradation of methylene blue on CsF_Coa, and Cs_Co NFs membranes (according to Eq. (1)) followed pseudo-first-order kinetics [1].

$$\ln\left(\frac{A_0}{A_t}\right) = kK = K_{app}t \quad (1)$$

where A_0 is the initial UV/visible spectrum of methylene blue, A_t is the UV/visible spectrum of methylene blue at illumination time t, k is the reaction rate constant, and K is the absorption coefficient of the reactant. A plot of $\ln(A_0/A_t)$ versus time shows a straight line whose slope is equal to the apparent rate constant *Kapp*. Percent degradation was calculated using Eq. (2) [12].

$$\text{Percent degradation} = 1 - \frac{A_t}{A_0} \quad (2)$$

5. Results and discussion

5.1. FTIR study

Fig. 4 shows the FTIR spectra of the Cs_P NFs membrane, the membranes involved in the different steps of the

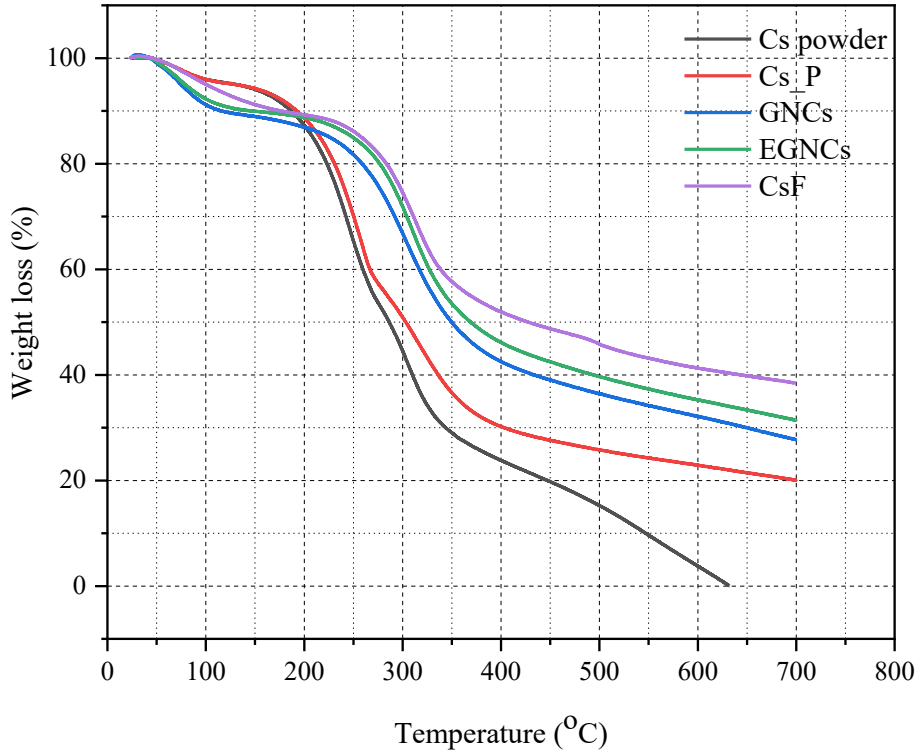

Fig. 6 – TGA of the NFs membranes involved in the func CS and functionalization process.

functionalization process (GCs, GNCs, and EGNCs), and the functionalized CsF NFs membrane (see Fig. 1). The spectrum of the Cs_P membrane showed a typical scissors vibration band at 1630 cm^{-1} for amine (-NH_2), a stretching band at 1680 cm^{-1} for the carbonyl carbon (C═O) of N-acetylcarbonyl and trifluoroacetate CF_3COO^-, and an intermediate band at 1538 cm^{-1} for the ammonium (-NH_3^+) ions [13–15]. The band that appeared at 1538 cm^{-1} was the result of salt formation between the $-NH_3^+$ ions of the Cs_P NFs membrane and the acetate (COO -) ions of the trifluoroacetic acid solvent. The salt formation between $-NH_3^+$ and COO^- ions has been widely documented in the literature [11]. In the spectrum of GCs NFs membrane. The intensity of the band at 1538 cm^{-1} for $-NH_3^+$ ions decreased slightly. The decrease in band intensity at 1538 cm^{-1} was attributed to the formation of C═N (imine) stretching bands [16]. The synthesis of imines between the free amines of Cs_P and aldehyde groups of GTA has been reported in the literature [17]. The spectrum GNCs NFs membrane exhibited only one scissors vibration band of the amine ((-NH_2) at 1630 cm^{-1}. The band at 1538 cm^{-1} for the $-NH_3^+$ ion disappeared completely, confirming our earlier argument for the formation of the C═N (imine) group [18,19]. The spectrum of EGNCs membrane showed bands in the range of 1000 and 1200 cm^{-1} and no change in the original positions of the other bands [20]. These bands could possibly be due to the C–O–C stretching of the cyclic ether, implying that the cyclic structure of the epoxide is maintained during the reaction [21]. The addition reaction of the amine group was carried out by ring opening of the terminal epoxide. This is evident from the fact that the C–O–C stretching band of the cyclic ether between 1000 and 1200 cm^{-1} shows a significant drop in the spectrum of the CsF NFs membrane [21]. The primary amine band at 1630 cm^{-1} broadens and shrinks slightly. The broadening could be due to two factors: first, the amine absorption is medium to high in this region due to N–H deformation and second, the stretching bands of C═O) and imine C═N overlap [22].

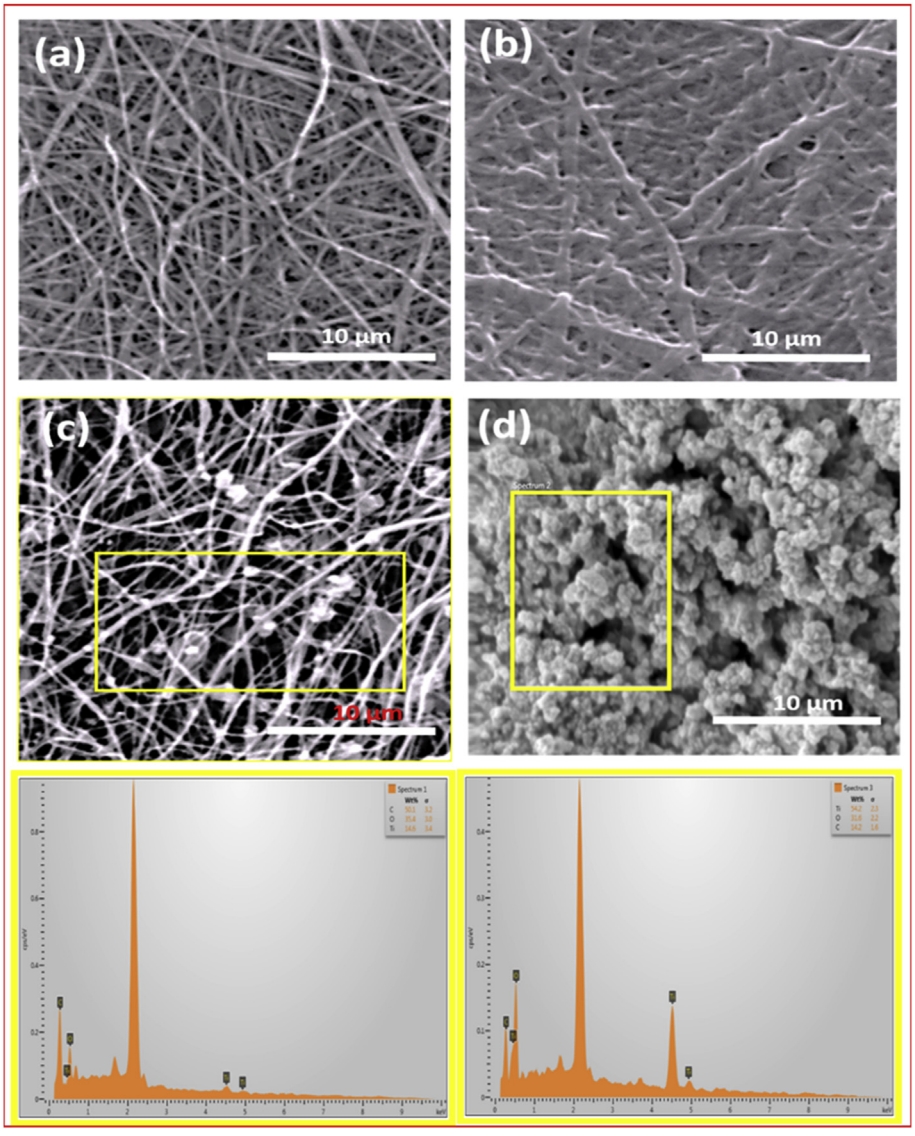

Fig. 7 – FESEM micrographs of the (a) Cs_P, (b) CsF, (c) Cs_Co, and (d) Cs_Coa NFs membrane. EDX spectra for the determination of Ti in Cs_Co, and Cs_Coa NFs membrane.

5.2. *XPS analysis*

Fig. 5 shows the XPS findings of the Cs_P and CsF NFs membranes. The O1s, N1s, and C1s spectra of both membranes are deconvoluted into separate peaks with different energies corresponding to their specific functionalities. For example, the O1s spectrum of the Cs_P NFs membrane can be convoluted into two peaks with binding energies of 532.9 eV corresponding to the C–O–C group of the Cs ring and 534.4 eV related to the C–O and C=O groups of the trifluoroacetate (TFA) and Cs [23]. The N1s spectrum of Cs_p NFs (Fig. 5a) showed a single peak with a binding energy of 402.5 eV,

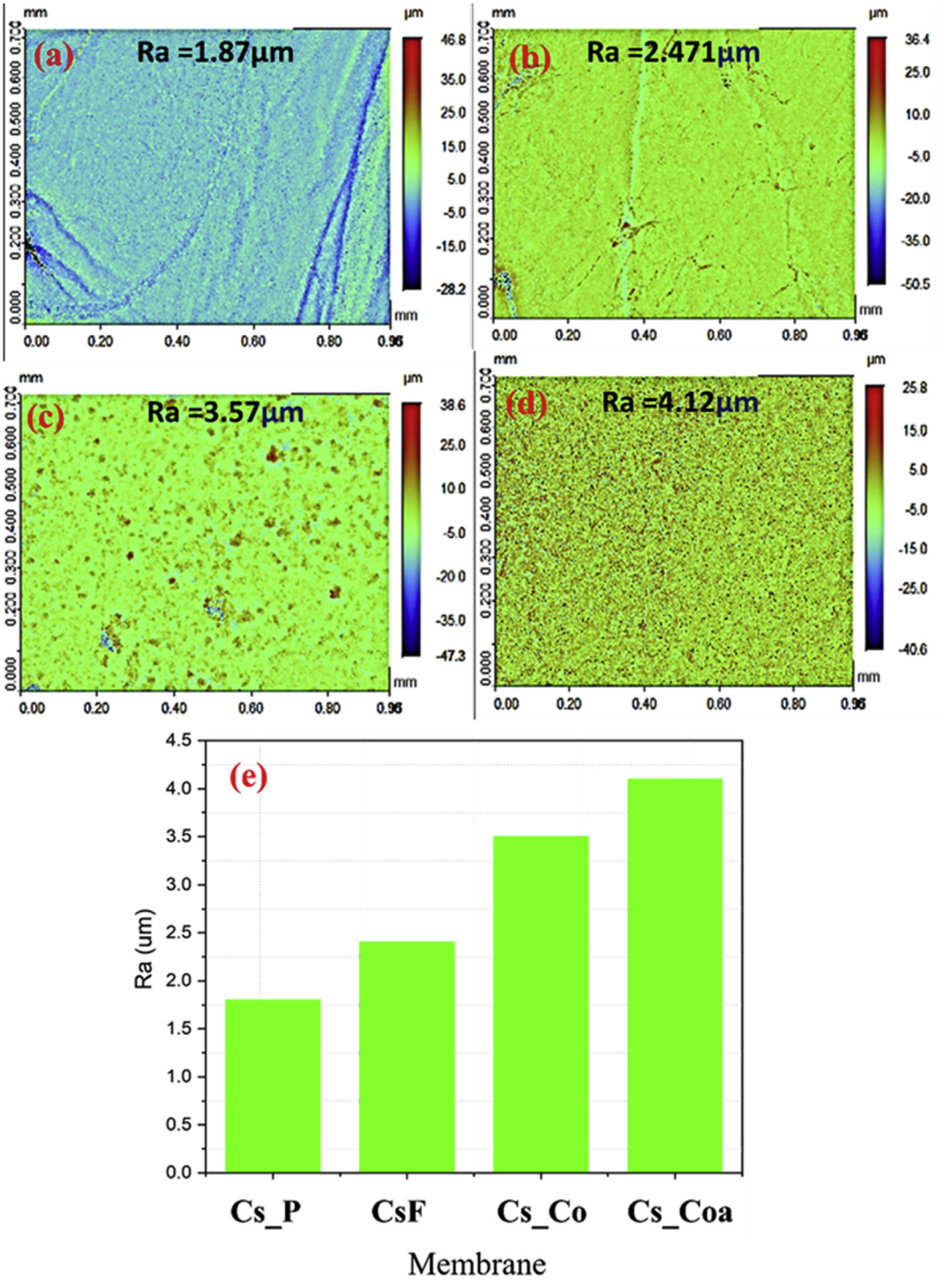

Fig. 8 – Surface roughness properties (a) Cs_P, (b) -CsF, (c) Cs_Co and (d) Cs_Coa NFs membranes, and (e) Comparative plot of the surface roughness of all the membranes.

attributed to the protonated amine species. The band of the protonated amine (-NH_3^+) at 1538 cm^{-1} is also discussed in FTIR (Fig. 4). This band is formed by the salt formation between -NH^{3+} ions of the Cs_P NFs membrane and COO^- ions of the TFA [13]. The C1 s spectrum of Cs_P NFs is deconvoluted into three peaks at 286.11, 287.76, and 289.31 eV, which are assigned to (C O/C N/C O–C), (C O), and (N C O), respectively. The (C O/C N/C O–C) peak is more pronounced than the others [24]. All the described peaks are present in the Cs_P NFs membrane, and the XPS results complement our FTIR explanation for the Cs_P NFs membrane. For the CsF NFs membrane, not only the number of peaks varied, but also the binding energies of the peaks in the O1s, N1s, and C1s spectra (Fig. 5b). For example, the O1s spectrum, is deconvoluted into four peaks. The two peaks with different intensities at a binding energy of 532.9 eV correspond to the C–O–C group of the Cs ring and the opening of the epoxide ring by the amine group [21]. A smaller peak at a binding energy of 531.5 eV corresponds to the O–H groups generated during the epoxide ring-opening reaction with amines. The binding peak at 533.8 eV corresponds to the C–O–H group, further confirms the ring-opening of the epoxide. The N1s spectra showed a single peak shifted to the binding energy of 399.8 eV, indicating nitrogen from amine groups. The appearance of this peak indicates the successful preparation of an amine-functionalized CsF NFs membrane [25]. The C1 s spectra

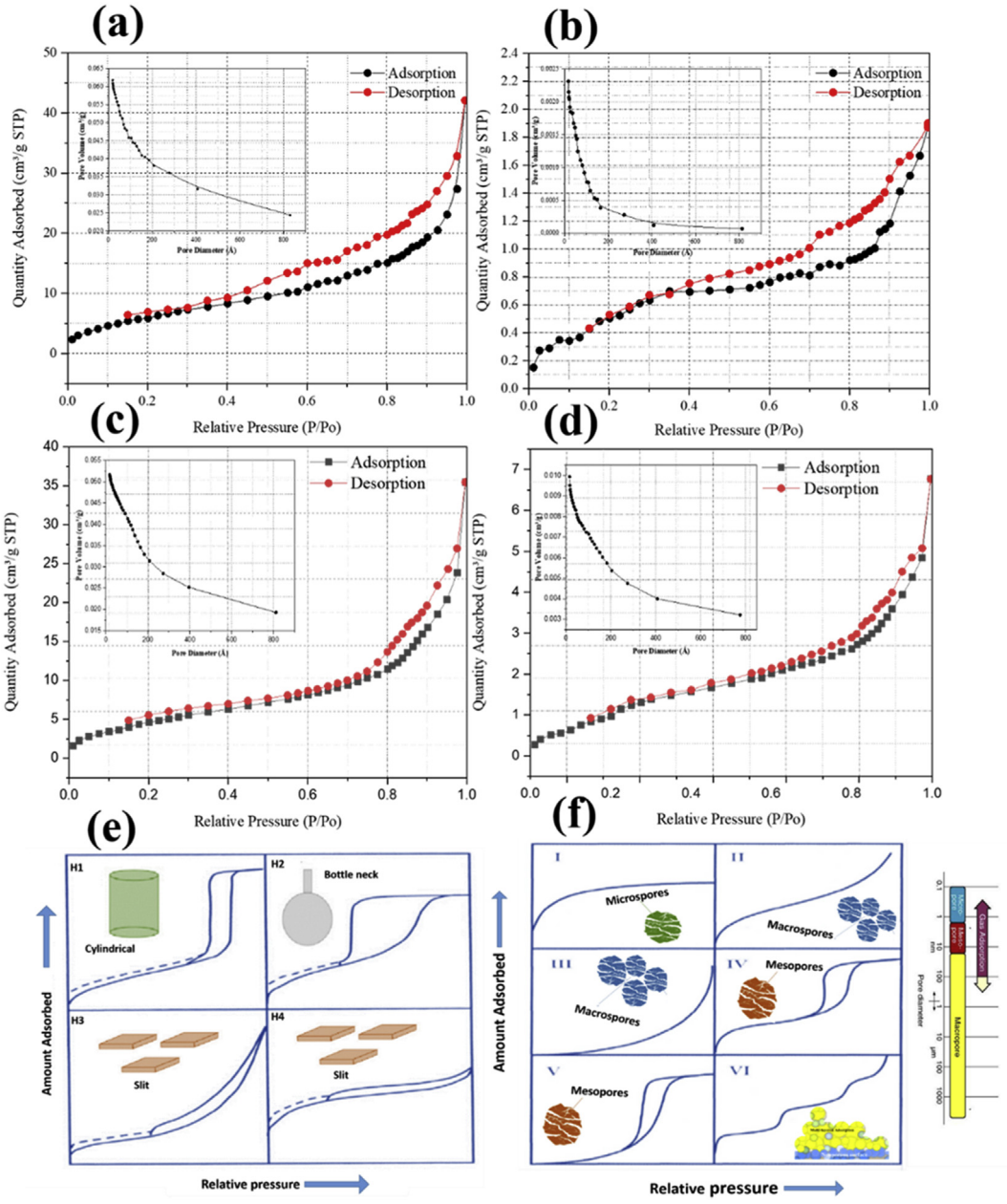

Fig. 9 – N_2 adsorption and desorption isotherm (a) Cs_P, (b) CsF, (c) Cs_Co, and (d) Cs_Coa NFs membranes. (e) Hysteresis model showing pore type and (f) Isotherm model showing pore size.

Table 1 – Determination of Surface area and porosity of the NFs membranes.

Samples name (NFs)	Surface area (m^2/g)	Pore volume (cm^3/g)	Pore size (A^O)	Total area in pores m^2/g
Cs_P	21.70	0.065	109.85	12.775
Cs_Co	18.30	0.054	119.85	9.851
CsF	2.17	0.003	44.05	1.086
Cs_Coa	4.90	0.011	84.90	2.113

showed two significant deconvoluted peaks with binding energies of 285.7 eV and 286.9 eV. The peak at 285.7 eV is related to the contribution of C–O and C– O–H functionalities [26], while the peak at 286.9 eV is related to C–O functionality [27]. The FTIR and XPS data confirm the fabrication of the CsF NFs membrane.

5.3. *TGA analysis of the functionalized NFs membrane*

Fig. 6 shows the thermal response of Cs powder, Cs_P NFs membrane, the membranes involved in the different functionalization steps (GNCs and EGNCs), and CsF NFs membrane (see Fig. 1). All membranes showed two phases of weight loss: The first occurred in the range of 30–100 °C, which was due to the evaporation of moisture. The second weight loss occurred in the range of 150–600 °C for Cs powder and Cs_P NFs membrane, while it was in the range of 200–700 °C for GNCs, EGNCs and CsF NFs membranes. The weight loss in the second phase was associated with the breakage of the deacetylated polysaccharide chains. However, the stabilities of these membranes were different. The maximum weight losses of the Cs powder and Cs_P NFs membranes occurred in the range of 150–400°C. The weight losses were ~75% and ~70%, respectively. The Cs powder completely decomposed up to 640 °C, but the Cs_P NFs membrane remained relatively stable at this temperature. The GNCs, EGNCs and CsF NFs membranes showed similar degradation in the of 200-400°C. The maximum weight loss for GNCs was ~59 % while the weight loss of the EGNCs NFs membrane was ~54%. CsF NFs membrane exhibited the least weight loss of ~48%. From results, it can be seen that the NFs membrane became thermally stable with each functionalization step. This could be due to the fact that the bond density between the polymer chains increased with increasing functional groups, resulting in more compact chemical structures. Therefore, it can be concluded that the CsF NFs membrane was more thermally stable than the others.

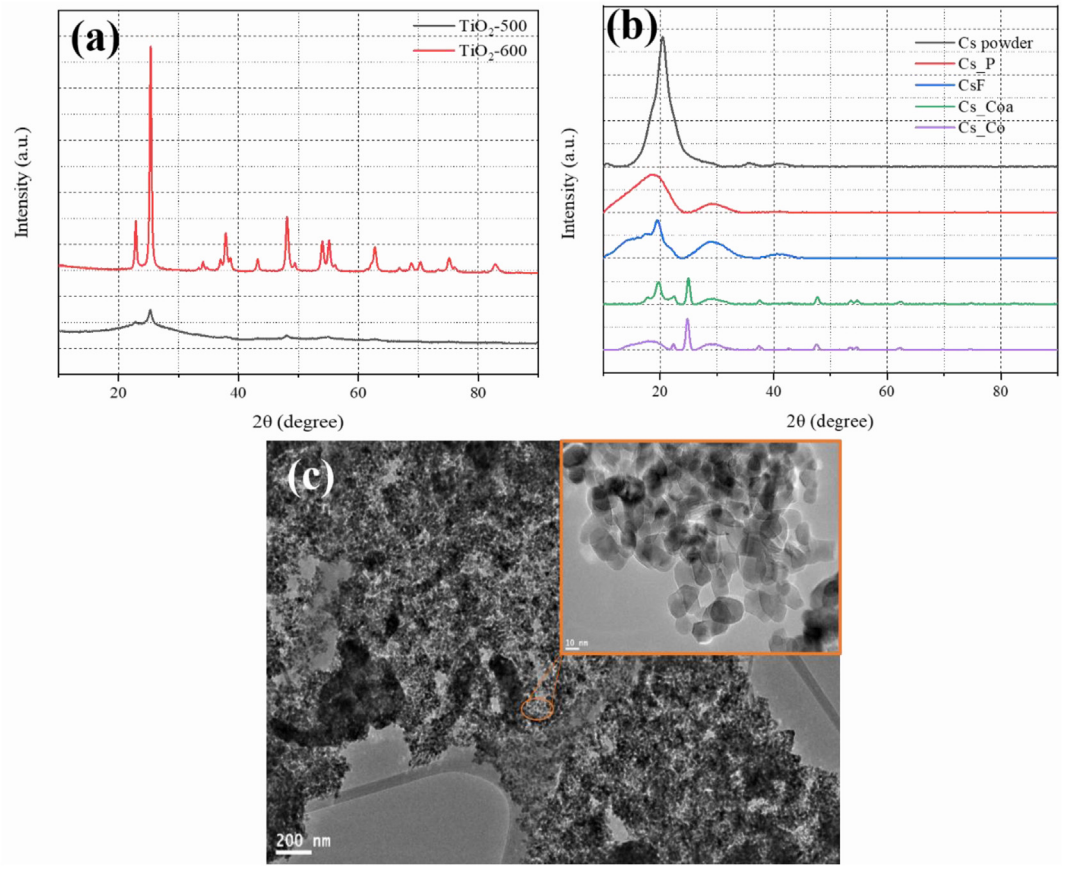

Fig. 10 – XRD of (a) TiO_2NPs, (b) Cs powder, Cs_P, CsF, Cs_Coa, and Cs_Co NFs membranes, and (c) TEM morphology of TiO_2 NPs.

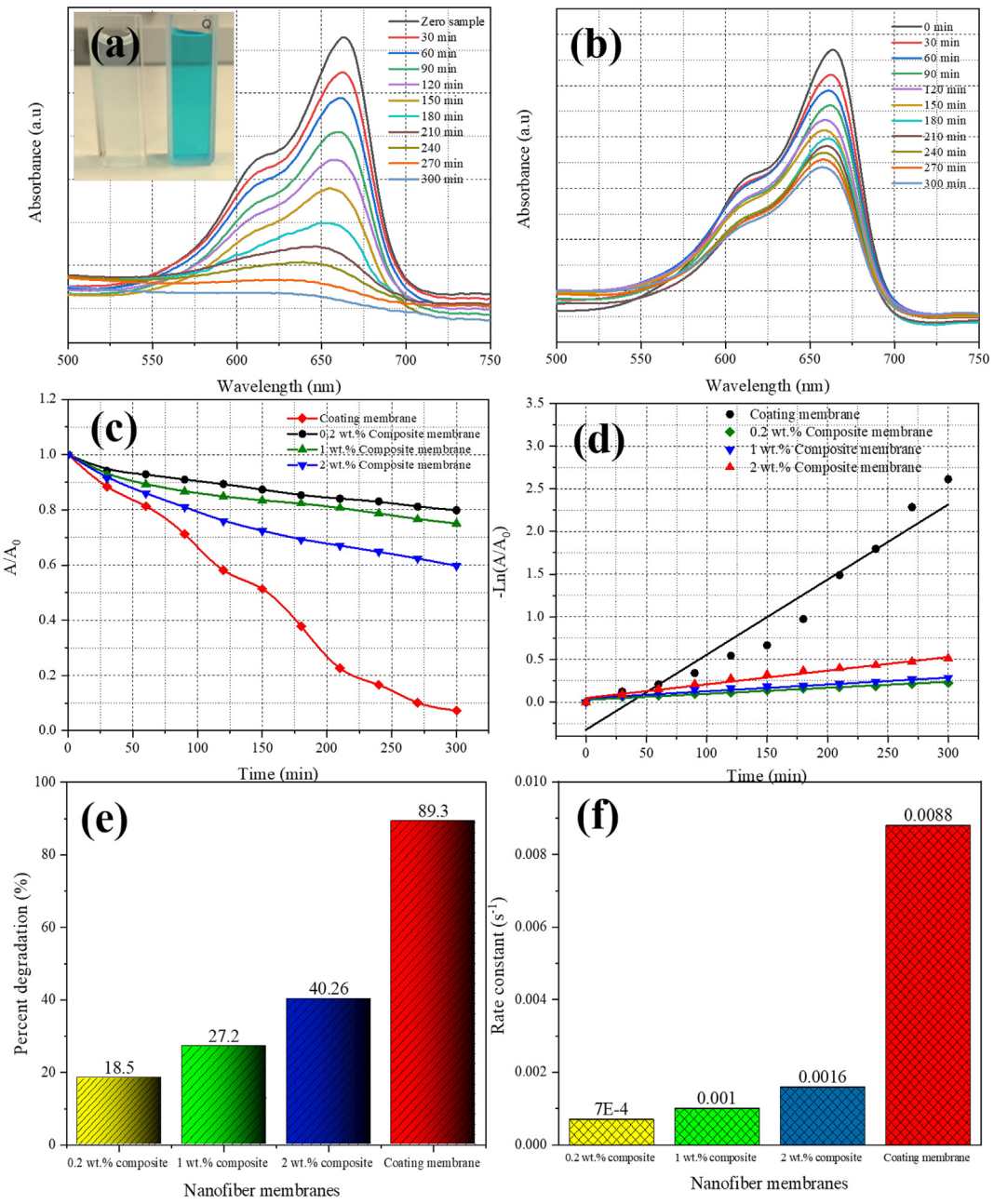

Fig. 11 – Photocatalytic degradation of methylene blue dye (constant dye concentration 10 ppm and membrane amount 100 used in each experiment), (a) absorption spectra of methylene blue dye induced by Cs_Coa and (b) absorption spectra methylene blue dye induced by Cs_Co (2wt% TiO_2/Cs composite) NFs membranes, (c) comparative A/A_o plot of the degradation of methylene blue for Cs_Coa and Cs_Co (with different wt% TiO_2NP_s), (d) kinetics, (e) % degradation and (f) rate constant.

5.4. *Morphology and surface roughness*

SEM micrographs of the Cs_P, CsF, Cs_Coa, and Cs_Co NFs membranes are shown in Fig. 7a–d. The morphology of the Cs_P NFs membrane was smooth and uniform. However, the morphology of the CsF NFs membrane became denser. This dense morphology of CsF NFs membrane could be attributed to the swelling of the NFs during the chemical reaction (Fig. 7b). When TiO_2 NPs were added to Cs_P without changing the electrospinning conditions, broken rolled fibers were observed as white patches on the Cs_Co NFs (Fig. 7c). These patches were caused by the addition of TiO_2 NPs, which increased the viscosity of the solution due to the physical crosslinking of the Cs chains. The change in viscosity of the polymer solution not only hindered the flow of the solution through the needle tip (polymer solution dries on the tip of the metallic needle and blocks it), but also affected the stretching of the charged jet, resulting in defective NFs [28,29].

Electrospraying of TiO_2 NPs on the CsF resulted in a thick cloud of TiO_2 NPs on its surface (Fig. 7d). The presence of the TiO_2 NPs in the Cs_Coa and Cs_Co NFs membrane is evident from the EDX data.

Fig. 8a–e shows the results of the surface profilometry of the Cs_p, CsF, Cs_Coa, and Cs_Co NFs membranes. The roughness of the surfaces of membranes increased after treatment and coating with TiO_2 NPs. The Cs_Coa NFs membrane (Fig. 6d) exhibited highest roughness, followed by the Cs_Co (Fig. 8c) and the CsF NFs membrane (Fig. 8b). The Cs_P NFs membrane exhibited lowest roughness (Fig. 8a). The higher surface roughness of the Cs_Coa NFs membrane (Fig. 8d) compared to other membranes might be due to the synergistic effect of chemical modification and random deposition of TiO_2 NPs on the NFs membrane surface. A similar increase in the surface roughness of the membranes due to the chemical modification [30] and the random deposition of TiO_2 NPs on the surface has been published in the literature [31]. In the case of the Cs_Co NFs membrane (Fig. 8c), the increase in roughness could be explained by the random dispersion of TiO_2 NPs in the polymer matrix [32].

5.5. *BET surface area and porosity*

The surface area and porosity of Cs_P, CsF, Cs_Coa, and Cs_Co NFs membranes were measured using nitrogen adsorption–desorption isotherms. BET is a well-known method for characterizing meso (diameter range 2–50 nm) and micro (diameter 2 nm) porous materials. The nitrogen adsorption–desorption isotherms for Cs_P, CsF, Cs_Coa, and Cs_Co NFs membranes are shown in Fig. 9a–f. The porosity of a material is often described as the ratio of the volume of pores and voids to the volume of the solid. The porosity of materials is defined by their adsorption properties. The International Union of Pure and Applied Chemistry (IUPAC) convention is a standard for classifying pore sizes based on nitrogen adsorption–desorption isotherms. There are six types of isotherms found in the literature that characterize the porosity of adsorbents. These include type I(microporous), II, III, and VI(non-porous or macroporous), and IV and V(mesoporous) [33–35]. Similarly, the hysteresis loop, which defines pore channels in materials is divided into four categories by IUPAC. For example, H1 represents porous materials with

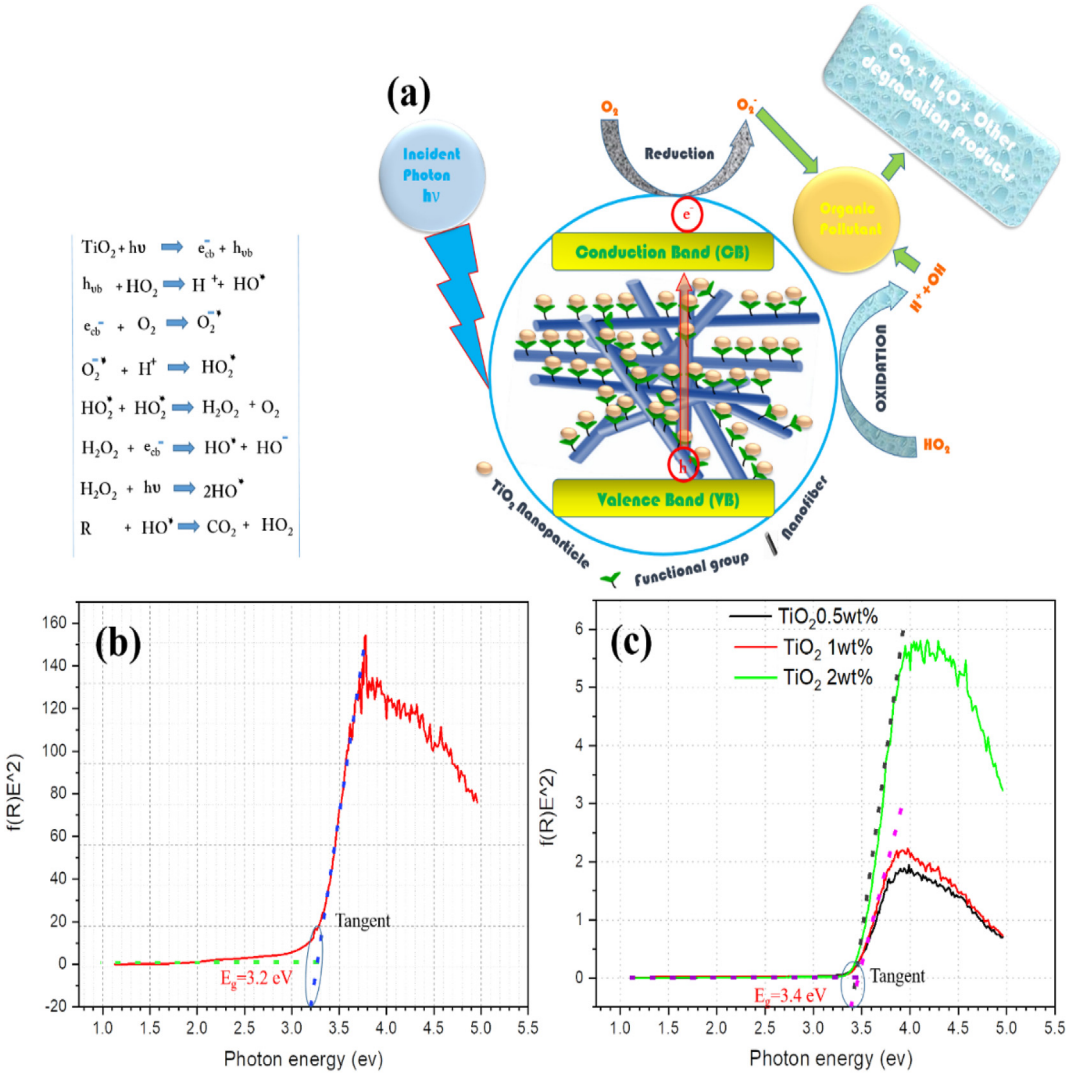

Fig. 12 – (a) Photocatalytic mechanism and energy band gaps of (b) Cs_Coa, and Cs_Co NFs membranes.

well-defined cylindrical pore channels or agglomerates of relatively uniform spheres, while H2 represents materials that are generally disordered and have an unclear distribution of pore size and shape, indicating bottlenecks or constrictions. H3 indicates slit pores, and H4 is often associated with narrow slit pores (Fig. 9e–f) [36]. The isotherms and hysteresis loop observed for the Cs_P and CsF, Cs_Coa, and Cs_Co NFs membranes were identical and were classified as IV isotherm and H3 hysteresis loop (IUPAC), corresponding to mesopores and slit pores, respectively. Similar observations for the pores of NFs membranes can also be found in the literature [37,38]. The surface area, pore-volume, pore size, and total area in pore of Cs_F and Cs_Coa NFs membranes significantly decreased compared to Cs_P and Cs_Co NFs membranes (Table 1). The decrease in surface area, pore-volume, pore size and total area in pore was attributed to NFs fusion caused by functionalization, in which the polymer chains collapsed due to the formation of hydrogen bonds between the functional groups in the polymer chains. This decrease was also favored by the TiO_2 coating.

5.6. *XRD and TEM analysis*

The XRD pattern was used to characterize TiO_2 NPs, Cs powder, Cs_P, CsF, Cs_Coa, and Cs_Co NFs membrane. The TiO_2 NPs were synthesized by the homogeneous precipitation method at 600 °C (Fig. 10a). The XRD pattern confirmed the existence of the anatase phase of the TiO_2 NPs. The Bragg diffractions of the TiO_2 NPs corresponded to the anatase phase characteristic crystal planes (101), (004), (200), (105), (211), (204), (116), (220), (215), and (303) (JCPDS-21-1272). The anatase phase of TiO_2 NPs is highly photoactive for water treatment [39]. The TEM images showed that the average particle size varied between 20 and 35 nm and the NPs tend to be spherical and highly crystalline (Fig. 10c). Cs powder generally shows two diffractions, one very small diffraction at ~ $2\theta = 12$ and the other intense diffraction at ~ $2\theta = 20°$. We will discuss the major diffraction at $2\theta = 20°$, which is related to the crystal II in the Cs structure. This diffraction is related to the allomorphic tendon. The characteristic sharp diffraction in the Cs powder becomes broader in Cs_P NFs membrane compared to the CsF and Cs_Coa NFs membranes (Fig. 10b). This indicates that the Cs_P NFs membrane has lost its crystallinity. This is attributed to the fact that the crystallinity of Cs in the powder form strongly depends on the arrangement of the chains packed in the crystalline structure [1,2]. The disturbance in regular packing of the chains created by the interaction between the ions in the Cs_P NFs with the ions of the solvent (already discussed in the FTIR and XPS sections) [40] might have affected the regular packing of the chains. The partial reduction in crystallinity of the CsF and Cs_Coa NFs membranes could be attributed to crosslinking and the introduction of amine groups into the NFs membranes. Similarly, the loss of crystallinity of Cs_Co could be attributed to crosslinking by TiO_2. The Ti–O bond in TiO_2 is polar. There is evidence that the polar oxygen of Ti–O has the potential to form hydrogen bonds with the polar hydrogen of the polymer. This leads to the formation of physical crosslinking [41]. A reduction in crystallinity due to crosslinking has been reported by Julkapli et al. [42,43].

5.7. *Photocatalytic study*

TiO_2, is one of the most studied semiconductor materials due to its low cost, photocatalytic activity, biocompatibility, non-toxicity, and excellent stability. It is available in various forms. These, include rutile, brookite, and anatase. The energy and gaps of rutile and anatase TiO_2 are 3.03 and 3.2 eV, respectively, and can be activated by photons in the near UV region (387 nm). A number of articles on the photocatalytic properties of TiO_2 with other ceramic particles are available in the literature. However, there is no information on the photocatalytic activity with polymers. There are few studies in which TiO_2 NPs have been used with NFs to achieve photocatalytic degradation of organic pollutants while minimizing their drawbacks such as spontaneous aggregation. Liang et al. have incorporated TiO_2 into carbon nanofibers (CNFs). In their study, they showed that CNFs half-wrapped in TiO_2 exhibited consistently strong photocatalytic activity against RB [44]. The photocatalytic abilities of electrospun Cs_Coa and Cs_Co NFs membranes were investigated using a UV light source to degrade a methylene dye in solution (Fig. 11a–f). Blank studies performed without the use of Cs_Coa and Cs_Co NFs membranes or a light source showed insignificant degradation of methylene blue. Fig. 11a–b shows the change in the absorption spectra of methylene blue dye by Cs_Coa and Cs_Co NFs membranes when exposed to UV light at regular time intervals at constant dose (100 mg) of the NFs membrane and concentration of the dye (10 ppm). The reduction of the unique absorption peak (the UV–visible absorption spectrum shows a peak at 663 nm, as reported, for the MB dye in solution) indicates that the methylene blue dye was significantly degraded over time by Cs_Coa and Cs_Co NFs membranes. The degradation efficiency of Cs_Coa and Cs_Co NFs membranes was 89.30% and 40.26%, respectively (Fig. 11c and e). Photocatalytic studies showed that the Cs_Coa NFs membrane exhibited higher photocatalytic efficiency. The reaction rate constant k of the Cs_Coa NFs membrane was 0.0088 min^{-1} and that of the Cs_Co NFs membrane was 0.0016 min^{-1}. The reaction rate constant of the Cs_Coa NFs membrane was higher than that the of Cs_Co NFs membrane (Fig. 11f). The results show that the Cs_Coa NFs membrane degrades methylene dye more efficiently when irradiated with UV light. Similar results were also found and reported in the literature [44]. The kinetic of the degradation followed first order kinetics in both cases (Fig. 11d). The photocatalytic activities of photocatalysts vary due to the differences in their photocatalytic physics and chemistry. Photocatalytic physics is mainly concerned with two physical variables. The first is light absorption, and the second is the generation and recombination of electrons and holes. The driving force of electron and hole transport is critical to photocatalytic chemistry. Since the energy band gaps of the Cs_Coa and Cs_Co NFs membranes are different (Fig 12b–c), the differences in the driving forces of electron

and hole transfer are the main reason, which means that the photocatalytic chemistry has a significant impact on their photocatalytic abilities. Another fact that supports the high photocatalytic activity of Cs_Coa NFs membrane is the adsorption of methylene blue on the membrane [45]. Moreover, the surface roughness (the Cs_Coa NFs membrane has high surface roughness (Ra 4.12 μm)) also improves the photocatalytic activity. The roughness leads to reflection of photons, which may result in increased photon absorption [46]. In conclusion, the better photocatalytic activity of the Cs_Coa NFs membrane is the result of a balance between the small band gap, surface roughness and smaller surface area [47].

6. Conclusions

We prepared a Cs NFs membrane by electrospinning, which was functionalized to CsF by our novel route. The CsF NFs membrane was then coated to produce Cs_Coa NFs membranes. A second NFs membrane was prepared by embedding TiO_2NPs in the fibers (Cs_Co). The Cs_Coa and Cs_Co NFs membranes were used to study their photocatalytic activities against methylene blue dye. FTIR analysis confirmed the incorporation of the new functional group into the Cs structure. XPS data confirmed the FTIR results and the fabrication of the CsF NFs membrane. SEM micrographs showed smooth morphology for the Cs_P NFs membrane and a denser morphology for the CsF NFs membrane (NFs swelled with functionalization). The SEM micrographs also showed a dense cloud of TiO_2 NPs on the surface of the Cs_Coa NFs membrane. TEM showed that the particle size of TiO_2 NPs varied between 20 and 35 nm and tended to be spherical. The XRD pattern confirmed the existence of the anatase phase of the TiO_2 NPs. The presence of Cs_Coa and Cs_Co NFs membranes was also confirmed by EDX. Surface profilometry confirmed an increase in the surface roughness of the CsF and Coa NFs membranes. BET analysis revealed that the isotherms and hystereses for all NFs membranes were of the IV and H3 types, respectively, corresponding to mesopores and slit pores. The higher photocatalytic activity of the Cs_Coa NFs membrane (89%) as compared to the Cs_Co NFs membrane (40%) was attributed to a balance between the short band gap, high surface roughness, and lower surface area.

Declaration of Competing Interest

There is no conflict of interest between the authors.

REFERENCES

[1] Tiwari DK, Behari J, Sen P. Application of nanoparticles in waste water treatment 1. 2008.

[2] Madaeni S, Ghaemi N, Alizadeh A, Joshaghani M. Influence of photo-induced superhydrophilicity of titanium dioxide nanoparticles on the anti-fouling performance of ultrafiltration membranes. Appl Surf Sci 2011;257:6175–80.

[3] Nor N, Jaafar J, Othman M, Rahman MA. A review study of nanofibers in photocatalytic process for wastewater treatment. Jurnal Teknologi; 2013. p. 65.

[4] Zheng X, Shen Z-p, Cheng C, Shi L, Cheng R, Dong J. Electrospinning Cu–TiO 2 nanofibers used for photocatalytic disinfection of bacteriophage f2: preparation, optimization and characterization. RSC Adv 2017;7:52172–9.

[5] Swaminathan M, Muruganandham M, Sillanpaa M. In: Hindawi, editor. Advanced oxidation processes for wastewater treatment; 2015.

[6] Zhang D, Li X, Tan H, Zhang G, Zhao Z, Shi H. Photocatalytic reduction of Cr (vi) by polyoxometalates/TiO2 electrospun nanofiber composites. RSC Adv 2014;4:44322–6.

[7] Wanag A, Sienkiewicz A, Rokicka-Konieczna P, Kusiak-Nejman E, Morawski AW. Influence of modification of titanium dioxide by silane coupling agents on the photocatalytic activity and stability. J Environ Chem Eng 2020;8:103917.

[8] Yang Y, Zhong H, Tian C. Photocatalytic mechanisms of modified titania under visible light. Res Chem Intermed 2011;37:91–102.

[9] Li J, Qiao H, Du Y, Chen C, Li X, Cui J. Electrospinning synthesis and photocatalytic activity of mesoporous TiO2 nanofibers. Sci World J 2012:2012.

[10] Ramasundaram S, Yoo HN, Song KG, Lee J, Choi KJ, Hong SW. Titanium dioxide nanofibers integrated stainless steel filter for photocatalytic degradation of pharmaceutical compounds. J Hazard Mater 2013;258:124–32.

[11] Haider S, Ali FAA, Haider A, Al-Masry WA, Al-Zeghayer Y. Novel route for amine grafting to chitosan electrospun nanofibers membrane for the removal of copper and lead ions from aqueous medium. Carbohydr Polym 2018;199:406–14.

[12] Iftikhar A, Yousaf S, Ali FAA, Haider S, Khan SUD, Shakir I. Erbium-substituted Ni0. 4Co0. 6Fe2O4 ferrite nanoparticles and their hybrids with reduced graphene oxide as magnetically separable powder photocatalyst. Ceram Int 2020;46:1203–10.

[13] Haider S, Park S-Y, Lee S-H. Preparation, swelling and electro-mechano-chemical behaviors of a gelatin–chitosan blend membrane. Soft Matter 2008;4:485–92.

[14] Mincheva R, Manolova N, Sabov R, Kjurkchiev G, Rashkov I. Hydrogels from chitosan crosslinked with poly (ethylene glycol) diacid as bone regeneration materials. E-Polymers 2004:4.

[15] Sangsanoh P, Supaphol P. Stability improvement of electrospun chitosan nanofibrous membranes in neutral or weak basic aqueous solutions. Biomacromolecules 2006;7:2710–4.

[16] Wang Z, Hu Q, Wang Y. Preparation of chitosan rods with excellent mechanical properties: one candidate for bone fracture internal fixation. Sci China Chem 2011;54:380–4.

[17] Schiffman JD, Schauer CL. Cross-linking chitosan nanofibers. Biomacromolecules 2007;8:594–601.

[18] Haider S, Al-Masry WA, Bukhari N, Javid M. Preparation of the chitosan containing nanofibers by electrospinning chitosan–gelatin complexes. Polym Eng Sci 2010;50:1887–93.

[19] Zhang Y, Venugopal J, Huang Z-M, Lim CT, Ramakrishna S. Crosslinking of the electrospun gelatin nanofibers. Polymer 2006;47:2911–7.

[20] Liu Y, Liu Y, Cao X, Hua R, Wang Y, Pang C. Biosorption studies of uranium (VI) on cross-linked chitosan: isotherm, kinetic and thermodynamic aspects. J Radioanal Nucl Chem 2011;290:231–9.

[21] Socrates G. Infrared and Raman characteristic group frequencies: tables and charts. John Wiley & Sons; 2004.

[22] Lewandowska K. Miscibility and thermal stability of poly (vinyl alcohol)/chitosan mixtures. Thermochim Acta 2009;493:42–8.
[23] Kehrer M, Duchoslav J, Hinterreiter A, Cobet M, Mehic A, Stehrer T. XPS investigation on the reactivity of surface imine groups with TFAA. Plasma Process Polym 2019;16:1800160.
[24] Zheng Z, Wei Y, Wang G, Gong Y, Zhang X. Surface characterization and cytocompatibility of three chitosan/polycation composite membranes for guided bone regeneration. J Biomater Appl 2009;24:209–29.
[25] Haider S, Al-zaghayer YS, Waheed A-M, Ali FAA, Hadj-Kali MK. Amine grafted chitosan nanofiber, method for preparation thereof and its use in heavy metal adsorption. Google Patents; 2016.
[26] Rojas J, Toro-Gonzalez M, Molina-Higgins M, Castano C. Facile radiolytic synthesis of ruthenium nanoparticles on graphene oxide and carbon nanotubes. Mater Sci Eng, B 2016;205:28–35.
[27] Dolgov A, Lopaev D, Lee CJ, Zoethout E, Medvedev V, Yakushev O. Characterization of carbon contamination under ion and hot atom bombardment in a tin-plasma extreme ultraviolet light source. Appl Surf Sci 2015;353:708–13.
[28] Haider S, Al-Zeghayer Y, Ali FAA, Haider A, Mahmood A, Al-Masry. Highly aligned narrow diameter chitosan electrospun nanofibers. J Polym Res 2013;20:1–11.
[29] Haider A, Haider S, Kang I-K. A comprehensive review summarizing the effect of electrospinning parameters and potential applications of nanofibers in biomedical and biotechnology. Arabian J Chemistry 2018;11:1165–88.
[30] Cabrera JN, Ruiz MM, Fascio M, D'Accorso N, Mincheva R, Dubois P. Increased surface roughness in polydimethylsiloxane films by physical and chemical methods. Polymers 2017;9:331.
[31] Chi L, Qian Y, Zhang B, Zhang Z, Jiang Z. Surface engineering and self-cleaning properties of the novel TiO 2/PAA/PTFE ultrafiltration membranes. Appl Petrochem Res 2016;6:225–33.
[32] Sakarkar S, Muthukumaran S, Jegatheesan V. Tailoring the effects of titanium dioxide (TiO2) and polyvinyl alcohol (PVA) in the separation and antifouling performance of thin-film composite polyvinylidene fluoride (PVDF) membrane. Membranes 2021;11:241.
[33] Sing KS. Reporting physisorption data for gas/solid systems with special reference to the determination of surface area and porosity (Recommendations 1984). Pure Appl Chem 1985;57:603–19.
[34] Broekhoff J. Mesopore determination from nitrogen sorption isotherms: fundamentals, scope, limitations. In: Studies in surface science and catalysis, vol. 3. Elsevier; 1979. p. 663–84.
[35] Thommes M, Kaneko K, Neimark AV, Olivier JP, Rodriguez-Reinoso F, Rouquerol J. Physisorption of gases, with special reference to the evaluation of surface area and pore size distribution (IUPAC Technical Report). Pure Appl Chem 2015;87:1051–69.
[36] Lowell S, Shields JE, Thomas MA, Thommes M. Characterization of porous solids and powders: surface area, pore size and density. Springer Science & Business Media; 2012.
[37] Han C, Zhang X, Ding C, Xiong S, Yu X, Wang Y. Improved performance of thin-film composite membrane supported by aligned nanofibers substrate with slit-shape pores for forward osmosis. J Membr Sci 2020;612:118447.
[38] Taha AA, Qiao J, Li F, Zhang B. Preparation and application of amino functionalized mesoporous nanofiber membrane via electrospinning for adsorption of Cr3+ from aqueous solution. J Environ Sci 2012;24:610–6.
[39] Wei X, Zhu G, Fang J, Chen J. Synthesis, characterization, and photocatalysis of well-dispersible phase-pure anatase TiO2 nanoparticles. Int J Photoenergy 2013:2013.
[40] Min L-L, Zhong L-B, Zheng Y-M, Liu Q, Yuan Z-H, Yang L-M. Functionalized chitosan electrospun nanofiber for effective removal of trace arsenate from water. Sci Rep 2016;6:1–12.
[41] Anaya-Esparza LM, Villagrán-de la Mora Z, Ruvalcaba-Gómez JM, Romero-Toledo R, Sandoval-Contreras T, Aguilera-Aguirre S. Use of titanium dioxide (TiO2) nanoparticles as reinforcement agent of polysaccharide-based materials. Processes 2020;8:1395.
[42] Julkapli NM, Ahmad Z, Akil HM. X-Ray diffraction studies of cross linked chitosan with different cross linking agents for waste water treatment application. In: AIP conference proceedings, vol. 1202. American Institute of Physics; 2010. p. 106–11. 1.
[43] Lou T, Wang X, Song G, Cui G. Synthesis and flocculation performance of a chitosan-acrylamide-fulvic acid ternary copolymer. Carbohydr Polym 2017;170:182–9.
[44] Liang Y, Zhou B, Li N, Liu L, Xu Z, Li F. Enhanced dye photocatalysis and recycling abilities of semi-wrapped TiO2@ carbon nanofibers formed via foaming agent driving. Ceram Int 2018;44:1711–8.
[45] Azeez F, Al-Hetlani E, Arafa M, Abdelmonem Y, Nazeer AA, Amin MO. The effect of surface charge on photocatalytic degradation of methylene blue dye using chargeable titania nanoparticles. Sci Rep 2018;8:1–9.
[46] Paz Y, Luo Z, Rabenberg L, Heller A. Photooxidative self-cleaning transparent titanium dioxide films on glass. J Mater Res 1995;10:2842–8.
[47] Colombo E, Li W, Bhangu SK, Ashokkumar M. Chitosan microspheres as a template for TiO 2 and ZnO microparticles: studies on mechanism, functionalization and applications in photocatalysis and H 2 S removal. RSC Adv 2017;7:19373–83.